Table 2. HRs of death by *PCDHB* methylation status in subgroup of known prognostic factors

Stratified by		*PCDHB* methylation	No. cases	No. deaths	HR* (95% CI)	*P*†
Overall		High	67	1	22.1 (5.3-93.4)	< 0.0001
(*n* = 140)		Low	73	2	1	
N-*myc* amplification	No	High	30	8	12.4 (2.6-58.9)	0.002
(*n* = 140)		Low	72	2	1	
	Yes	High	37	20	NE	—
		Low	1	0		
TrkA overexpression	Yes	High	20	6	18.3 (2.2-152.6)	0.007
(*n* = 130)		Low	49	1	1	
	No	High	40	19	NE	
		Low	21	0		
DNA ploidy	Aneuploid	High	17	5	18.3 (2.1-156.7)	0.008
(*n* = 125)		Low	49	1	1	
	Diploid	High	38	17	NE	
		Low	21	0		
Clinical stages	Stages I, II,	High	8	0	NE	—
(*n* = 140)	and IVS	Low	52	0		
	Stages III	High	59	28	7.4 (1.8-31.3)	0.006
	and IV	Low	21	2	1	
Age at diagnosis	<1	High	11	3	NE	
(*n* = 140)	≥1	Low	59	0		
		High	56	25	4.5 (1.1-18.9)	0.043
		Low	14	2	1	

*HR of death for a case with high *PCDHB* methylation compared with a case with low methylation. NE shows not estimable due to no events in at least one category.
†Significance level for a high *PCDHB* methylation to low methylation using Cox proportonal model.

methylation. Second, methylation of the *PCDHB* family did not affect gene expression, and there should have been no selection of cells with the *PCDHB* methylation, in contrast to the case of promoter methylation of tumor suppressor genes. Investigation into the mechanism of the intrinsic tendency for methylation of multiple CGIs is necessary. Furthermore, alleviation of the intrinsic tendency could block progression of neuroblastomas and have potential therapeutic value.

Among the six CGI (groups) outside promoter regions analyzed here, CIMP in neuroblastomas preferentially affected four CGI (groups); those of the *PCDHB* family, the *PCDHA* family, *HLP*, and *CYP26C1*. Unexpectedly, three CGIs that are known to be frequently methylated in human colon cancers with CIMP, MINT1, MINT2, and MINT17 (16) were not methylated in neuroblastoma cell lines (data not shown). Among the nine CGIs in promoter regions analyzed, CIMP in neuroblastomas affected only three, those of *RASSF1A*, *BLU*, and *DKFZp451I127*. The nine CGIs were selected based upon previous reports as tumor suppressor genes (*RASSF1A*, *BLU*, *p16*, and *hMLH1*; refs. 21–23), the chromosomal location flanking the *PCDHB* family (*PCDHB1* and *TAF7*), our previous report on the fidelity in inheriting methylation patterns (*p41Arc* and *SIM2*; ref. 19), and the findings here (*DKFZp451I127*). Because gene expression and possibly chromatin structures affect the frequency of *de novo* methylation (24, 25), the available data suggest that CGIs useful to sensitively detect CIMP might vary according to the tumor type.

The influence of CIMP on prognosis was here found to be comparable to that of the currently most reliable marker, N-*myc* amplification, and stronger than *TrkA* overexpression and DNA ploidy on univariate analysis. Subgroup analysis showed that the influence was independent of *TrkA* overexpression, DNA ploidy and age at diagnosis and CIMP had influence even in cases without N-*myc* amplification and in advanced stages. These points strongly indicated CIMP to be a promising new prognostic marker. However, the cutoff values adopted here are tentative, and the HRs obtained could have been overestimated. A validation study using independent samples is necessary for further evaluation. The fact that cases with CIMP contained almost all the cases with N-*myc* amplification suggested that a common molecular mechanism caused both alterations, or that CIMP may lead to N-*myc*

amplification. Whatever the case, the findings might provide clues to molecular mechanisms of neuroblastoma development.

In summary, the present study showed that CIMP is present specifically in neuroblastomas with poor prognosis and that can be sensitively detected by focusing on *PCDHB* methylation. CIMP seems to be a promising new prognostic marker, and its evaluation and investigations into the mechanisms underlying CIMP in neuroblastomas seem warranted.

Acknowledgments

Received 7/27/2004; revised 11/14/2004; accepted 11/24/2004.

Grant support: Grant-in-aid for the Third-term Cancer Control Strategy Program from the Ministry of Health, Labour, and Welfare, Japan and Research Resident Fellowship from the Foundation for Promotion of Cancer Research (M. Abe).

The costs of publication of this article were defrayed in part by the payment of page charges. This article must therefore be hereby marked advertisement in accordance with 18 U.S.C. Section 1734 solely to indicate this fact.

We thank Drs. E. Okochi-Takada and G. S. Goldberg for critical reading of the article and the institutions for participation in the collection of clinical materials.

References

1. Jones PA, Baylin SB. The fundamental role of epigenetic events in cancer. Nat Rev Genet 2002;3:415–28.
2. Chen RZ, Pettersson U, Beard C, Jackson-Grusby L, Jaenisch R. DNA hypomethylation leads to elevated mutation rates. Nature 1998;395:89–93.
3. Kondo Y, Kanai Y, Sakamoto M, et al. Genetic instability and aberrant DNA methylation in chronic hepatitis and cirrhosis-A comprehensive study of loss of heterozygosity and microsatellite instability at 39 loci and DNA hypermethylation on 8 CpG islands in microdissected specimens from patients with hepatocellular carcinoma. Hepatology 2000;32:970–9.
4. Ushijima T, Morimura K, Hosoya Y, et al. Establishment of methylation-sensitive-representational difference analysis and isolation of hypo- and hypermethylated genomic fragments in mouse liver tumors. Proc Natl Acad Sci U S A 1997;94:2284–9.
5. Kaneda A, Takai D, Kaminishi M, Okochi E, Ushijima T. Methylation-sensitive representational difference analysis and its application to cancer research. Ann N Y Acad Sci 2003;983:131–41.
6. Takai D, Yagi Y, Wakazono K, et al. Silencing of *HTR1B* and reduced expression of *EDN1* in human lung cancers, revealed by methylation-sensitive representational difference analysis. Oncogene 2001; 20:7505–13.
7. Kaneda A, Kaminishi M, Yanagihara K, Sugimura T, Ushijima T. Identification of silencing of nine genes in human gastric cancers. Cancer Res 2002;62:6645–50.
8. Miyamoto K, Asada K, Fukutomi T, et al. Methylation-associated silencing of heparan sulfate *D-glucosaminyl 3-O-sulfotransferase-2* (*3-OST-2*) in human breast, colon, lung and pancreatic cancers. Oncogene 2003;22:274–80.
9. Hagihara A, Miyamoto K, Furuta J, et al. Identification of 27 5′ CpG islands aberrantly methylated and 13 genes silenced in human pancreatic cancers. Oncogene 2004;23:8705–10.
10. Brodeur GM. Neuroblastoma: biological insights into a clinical enigma. Nat Rev. Cancer 2003;3:203–16.
11. Schwab M, Westermann F, Hero B, Berthold F. Neuroblastoma: biology and molecular and chromosomal pathology. Lancet Oncol 2003;4:472–80.
12. Nakagawara A, Arima-Nakagawara M, Scavarda NJ, et al. Association between high levels of expression of the *TRK* gene and favorable outcome in human neuroblastoma. N Engl J Med 1993;328:847–54.
13. Jaenisch R, Bird A. Epigenetic regulation of gene expression: how the genome integrates intrinsic and environmental signals. Nat Genet 2003;33:245–54.
14. Li E. Chromatin modification and epigenetic reprogramming in mammalian development. Nat Rev Genet 2002;3:662–73.
15. Kaneda A, Kaminishi M, Sugimura T, Ushijima T. Decreased expression of the seven ARP2/3 complex genes in human gastric cancers. Cancer Lett 2004; 212:203–10.
16. Toyota M, Ahuja N, Ohe-Toyota M, et al. CpG island methylator phenotype in colorectal cancer. Proc Natl Acad Sci U S A 1999;96:8681–6.
17. Gonzalgo ML, Hayashida T, Bender CM, et al. The role of DNA methylation in expression of the *p19/p16* locus in human bladder cancer cell lines. Cancer Res 1998;58:1245–52.
18. Nguyen C, Liang G, Nguyen TT, et al. Susceptibility of nonpromoter CpG islands to *de novo* methylation in normal and neoplastic cells. J Natl Cancer Inst 2001; 93:1465–72.
19. Ushijima T, Watanabe N, Okochi E, et al. Fidelity of the methylation pattern and its variation in the genome. Genome Res 2003;13:868–74.
20. Yamashita K, Dai T, Dai Y, Yamamoto F, Perucho M. Genetics supersedes epigenetics in colon cancer phenotype. Cancer Cell 2003;4:121–31.
21. Agathanggelou A, Dallol A, Zochbauer-Muller S, et al. Epigenetic inactivation of the candidate 3p21.3 suppressor gene *BLU* in human cancers. Oncogene 2003; 22:1580–8.
22. Takita J, Hayashi Y, Nakajima T, et al. The *p16* (*CDKN2A*) gene is involved in the growth of neuroblastoma cells and its expression is associated with prognosis of neuroblastoma patients. Oncogene 1998; 17:3137–43.
23. Harada K, Toyooka S, Maitra A, et al. Aberrant promoter methylation and silencing of the *RASSF1A* gene in pediatric tumors and cell lines. Oncogene 2002; 21:4345–9.
24. De Smet C, Loriot A, Boon T. Promoter-dependent mechanism leading to selective hypomethylation within the 5′ region of gene *MAGE-A1* in tumor cells. Mol Cell Biol 2004;24:4781–90.
25. Richards EJ, Elgin SC. Epigenetic codes for heterochromatin formation and silencing: rounding up the usual suspects. Cell 2002;108:489–500.

Journal of Medical Systems, Vol. 29, No. 6, December 2005 (© 2005)
DOI: 10.1007/s10916-005-6134-0

Improving Precise Positioning of Surgical Robotic Instruments by a Three-Side-View Presentation System on Telesurgery

Kenta Hori,[1,7] Tomohiro Kuroda,[2] Hiroshi Oyama,[3] Yasuhiko Ozaki,[4] Takehiko Nakamura,[5] and Takashi Takahashi[6]

For faultless collaboration among the surgeon, surgical staffs, and surgical robots in telesurgery, communication must include environmental information of the remote operating room, such as behavior of robots and staffs, vital information of a patient, named supporting information, in addition to view of surgical field. "Surgical Cockpit System," which is a telesurgery support system that has been developed by the authors, is mainly focused on supporting information exchange between remote sites. Live video presentation is important technology for Surgical Cockpit System. Visualization method to give precise location/posture of surgical instruments is indispensable for accurate control and faultless operation. In this paper, the authors propose three-side-view presentation method for precise location/posture control of surgical instruments in telesurgery. The experimental results show that the proposed method improved accurate positioning of a telemanipulator.

KEY WORDS: telesurgery; robotic surgery; Surgical Cockpit System; three-side-view; precise instruments positioning.

INTRODUCTION

In telesurgery, a teleoperating surgeon to operate a surgical robot placed in a room, called "operator site," is spatially separated from a patient and other surgical staffs in a remote operating room, called "operation site," and information network connecting the two sites enable the surgeon to operate the patient. The surgeon

[1]Graduate School of Informatics, Kyoto University, Kyoto, Japan.
[2]Department of Medical Informatics, Kyoto University Hospital, Kyoto, Japan.
[3]Graduate School of Medicine, The University of Tokyo, Tokyo, Japan.
[4]Research and Development Headquarters, NTT Data Corporation, Tokyo, Japan.
[5]Department of Neurosurgery, Fukui Red Cross Hospital, Fukui, Japan.
[6]Advanced Software Technology & Mechatronics Research Institute of Kyoto, Kyoto, Japan.
[7]To whom correspondence should be addressed at Kyoto University Cell/Biodynamics Simulation Center, Kyoto Research Park, Building 4 8F, 93, Chudoji Awata-cho, Shimogyo, Kyoto 600 8815, Japan; e-mail: hori@biosim.med.kyoto-u.ac.jp.

needs to understand motion of surgical instruments, conditions of the patient, and other status in the operation site. For faultless collaboration among the surgeon, surgical staffs, and surgical robots in telesurgery, communication must include environmental information of the operating site, such as behavior of robots and staffs, vital information of a patient, named supporting information, in addition to view of surgical field.

The authors have been developing a telesurgery support system named "Surgical Cockpit System"(Fig. 1).[1] The Surgical Cockpit System consists of three fundamental subsystems, operating-field subsystem, robot subsystem, and surgical-environment subsystem. The operating-field subsystem provides view around operating-field and target organs. The robot subsystem supports manipulation of surgical robots, teleinstruction tools, and other tools for telesurgery. The surgical-environment subsystem, the peculiarity of the Surgical Cockpit System, provides multipurpose information display, which visualizes any kinds of additional information such as panoramic view of the operating room, multiangle presentation of the target of the patient, virtual surgeon guides, vital information of the patient, and so on. In this report, methodology of live video presentation is discussed for information supporting on the surgical-environment subsystem.

To obtain precise location/posture of surgical instruments relative to target is indispensable for accurate control and faultless operation. Therefore, visualization method to give precise location/posture plays important role in telesurgery support system. Foregoing research of the authors proposed to integrate two types of view, that is, detailed view of the target and wide-angle view around the target.[1] Experimental results show effectiveness of the proposed method for roughly positioning of the end effector and detailed approach. However, location/posture control of surgical instruments is quite difficult on the former method. It is because to recognize current location/posture of surgical instruments is quite difficult under single view environment provided by former prototype (Fig. 2).

The purpose of this paper is to propose multiview system for precise location/posture control of surgical instruments in telesurgery, and evaluate the effect of proposed method.

METHODS

This study proposes to use three-side-view presentation in addition to circumstantial view for supporting location/posture recognition, and evaluate effectiveness of three-side-view presentation on telerobotic operation.

To present the depth of the target to a teleoperating surgeon, multiangle presentation is required. A three-side-view method is a multiangle presentation method mainly used for solid shape design. Three-side-view consists of front view, side view, and top view. Three-side-view presentation for telerobotic surgery eases recognition of relative posture between target organ and surgical instruments.

In this research, three-side-view was applied for presenting relative posture around operating-field. Live video images of the operating field and the operating table were integrated into a multiplexed image with four segments; three segments

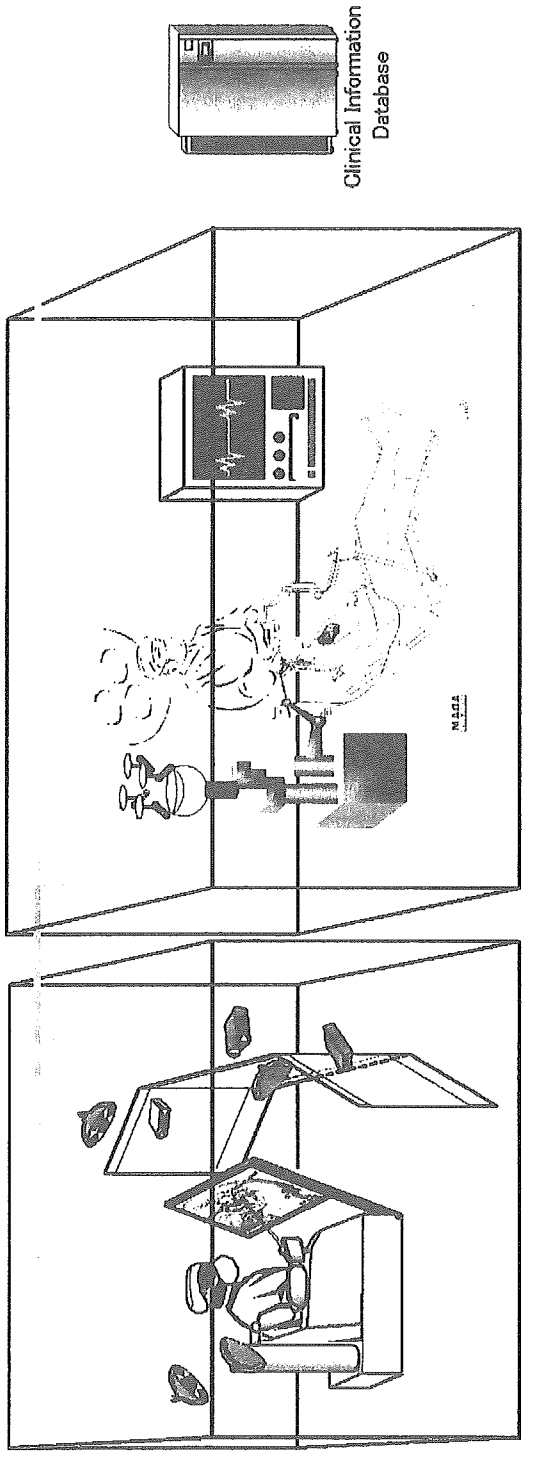

Fig. 1. Concept of Surgical Cockpit System.

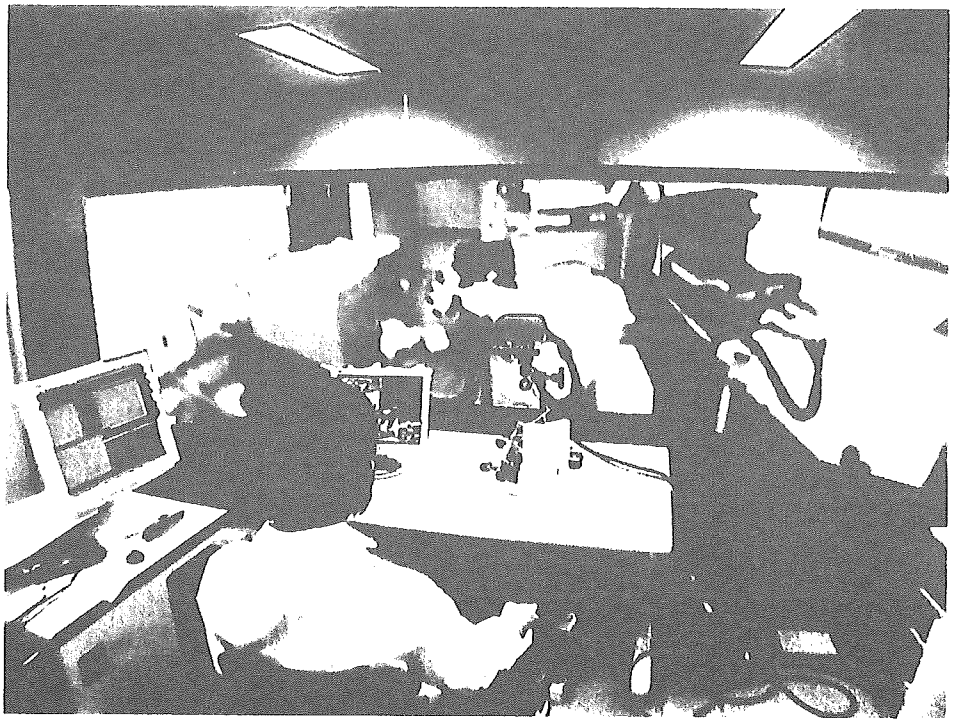

Fig. 2. Single view environments in Surgical Cockpit System.

were used to display three-side-view and the other segment was used to display around an operating table (Fig. 3). For evaluating three-side-view presentation, the proposed method was compared with wide-view immersive presentation around an operating table, which is proposed in the foregoing research. The conditions of presentation method in the experiment were named wide-immersive mode and three-side-view mode. In wide-immersive mode, enlarged live video by a wide-angle camera was displayed on multidisplay system with three screens placed side by side (Fig. 2). The size of each screen is 60 inches. The resolution is SXGA (1280 × 1024). Live video was captured and mapped on a virtual rectangular screen by OpenGL function to display enlarged video. The format of video signal is NTSC. In three-side-view mode, multiplexed image was displayed on a center screen of three side-by-side screens used in wide-immersive mode. Detailed view of operating field was provided by operating-field subsystem.

The evaluation was performed under delayed-video conditions. Subjects were 5th grade students of medical school of Kyoto University. The conditions of video streaming delay were no-delay condition and satellite condition. In no-delay condition, live video was presented without delay. In satellite condition, delay consisted of MPEG-2 encoding/decoding delay and satellite communication delay. The measurement of MPEG-2 encoding and decoding time shows that the delay of MPEG-2 encoding and decoding is about 500 ms. Round trip time from Kyoto University,

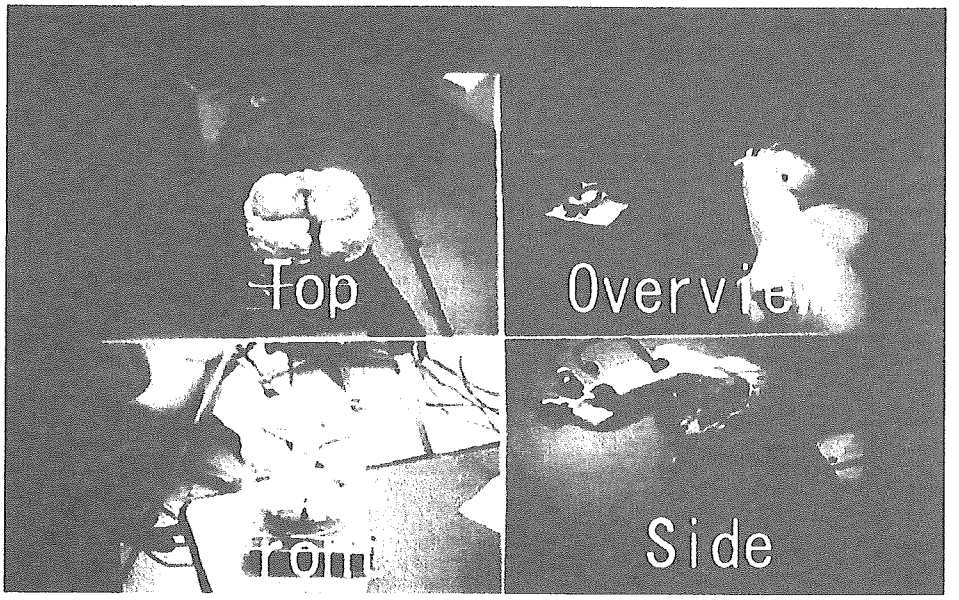

Fig. 3. Three-sides-view of operating field.

Kyoto, Japan, to Institut of Teknologi Bandung, Bandung, Indonesia, which is connected over satellite communication served by AI3 project[2] shows that approximate transmission delay over satellite communication is 250 ms. Therefore, the satellite-communication delay was decided to be 250 ms. Total delay on satellite condition was 750 ms. The delay was artificially appended by a delay generator between MPEG-2 encoder and decoder (Fig. 4).

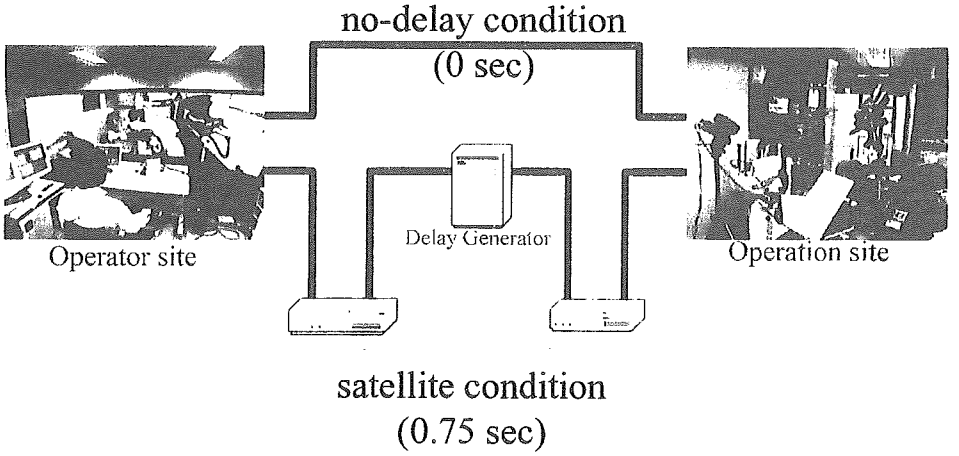

Fig. 4. Delay condition of the experiment.

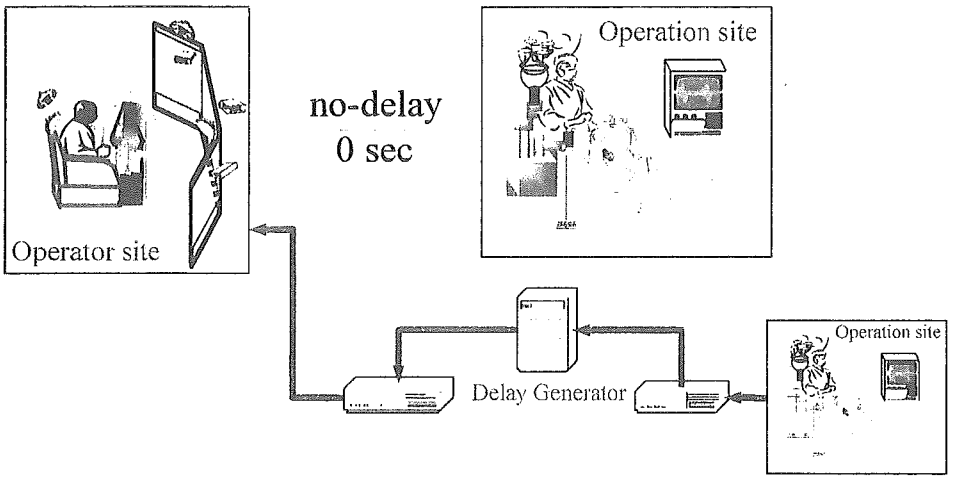

Fig. 4. Continued.

The experimented conditions were four combined conditions of presentation modes and network delay conditions, wide-immersive mode with no-delay condition (WN), wide-immersive mode with satellite condition (WS), three-side-view mode with no-delay condition (TN), and three-side-view mode with satellite condition (TS).

A task scenario of the experiment was a target-pointing task that assumes centesis. Each subject tried to apply tip of an instrument to a target area. The target area was 1.5 cm in diameter (Fig. 5). Each subject was instructed to adjust an instrument perpendicularly on the target area.

Four conditions were evaluated by comparing posture of an instrument at the end of the task (final posture), time to finish the task (task achievement time) among the four conditions, and by sensory evaluation of the subjects.

The final posture was evaluated by error angle between the normal line on the target area and the direction of the instrument in the final posture. The task achievement time was defined as time whole process time of the task. Final posture and task achievement time were analyzed with nonparametric test by SPSS. Rejection ratio was 0.05.

In the sensory evaluation, incongruous sense of given view, drivability of the robot, and easiness of spatial recognition were evaluated by cyclic paired comparison. The cyclic paired comparison is a paired comparison method with minimum sets of compared pairs.[3] For the cyclic paired comparison, evaluated conditions should be compared in cyclic order. In the experiment, the order of conditions was {WN, WS, TS, TN, WN}. The last WN condition could be used to evaluate learning effect for evaluation of final posture and task achievement time.

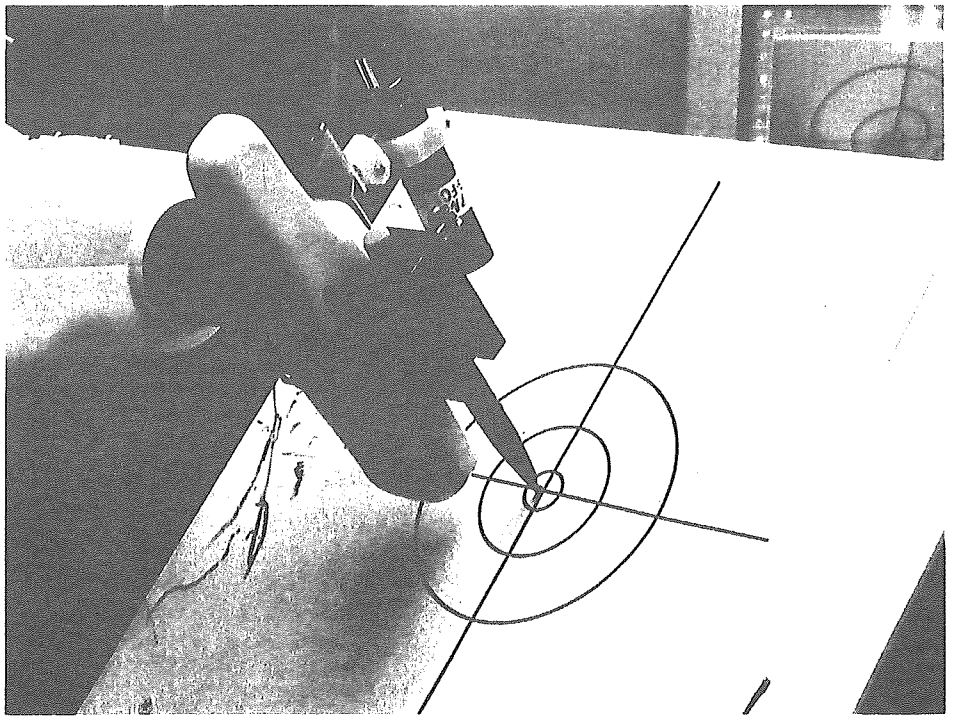

Fig. 5. Target positioning task in the experiment.

RESULTS

For final posture, conditions of presentation methods were statistically different in error angle of the final posture (Fig. 6(a), (b)). The error angles under three-side-view modes were significantly smaller than results under wide-immersive modes for each of no-delay condition and satellite condition. As per the results, the three-side-view presentation was good at the accurate control of the instrument posture.

For task achievement time, each set of conditions {WS, TS} and {WN (first), TN} had no statistical difference (Fig. 7(a), (b)). The task achievement time under TN conditions was significantly longer than the last WN condition (Fig. 7(a)). The first WN condition and the last WN condition were statistically different in task achievement time. The results show that learning effects affected task achievement time through the experiment. On the other hand, conditions of presentation methods did not affect for task achievement time.

By sensory evaluation, orders in each set of {WN, TN} and {WS, TS} were observed for incongruous sense of given view, drivability of the robot, and easiness of spatial recognition (Fig. 8).

For incongruous sense of given view (Fig. 8(a)), significant differences were not confirmed in both sets of {WN, TN} and {WS, TS}. However, WN conditions were a little more incongruous than TN conditions, and WS conditions were a little more

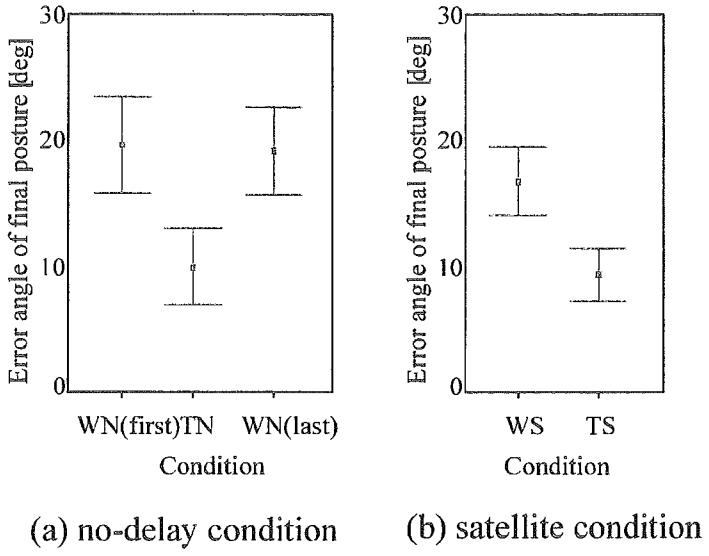

Fig. 6. The results of error angle of final posture.

incongruous than TS conditions. In conclusion, the three-side-view presentation was not significant but a little more effective than the wide-immersive presentation.

For drivability of the robot (Fig. 8(b)), each set of {WN, TN} and {WS, TS} was at similar order on the observed order. The results showed that three-side-view presentation was not effective for drivability of the robot. Significant differences were not confirmed. Impressions of the subjects show that much relative location/posture

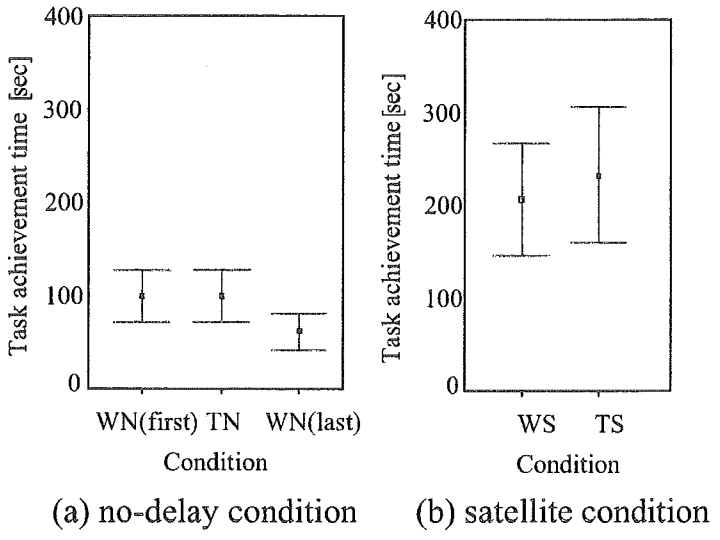

Fig. 7. The results of task achievement time.

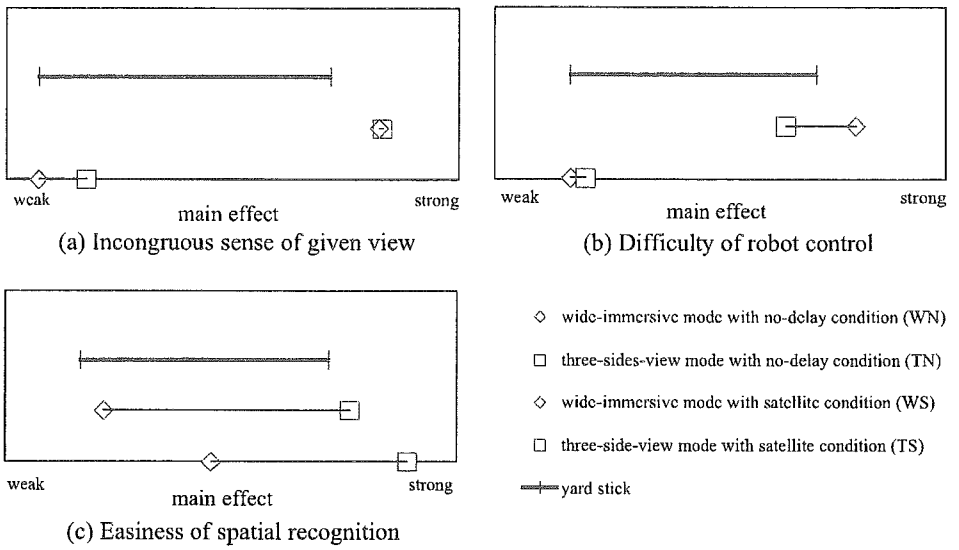

Fig. 8. The result for sensory evaluation.

information was provided in the three-side-view presentation; however surplus information increased the complexity of the given view. In the three-side-view presentation, the display area was divided into four sections. The display layout was complex and the display size for one camera view was reduced.

For easiness of spatial recognition (Fig. 8(c)), TN conditions tended to be a little easier than WN conditions, and TS conditions tended to be a little easier than WS conditions. In both sets significant differences were not confirmed. The results show that the three-side-view presentation was not significant but a little easier for spatial recognition than the wide-immersive presentation.

The results and the impressions showed that the spatial recognition could be difficult by the view complexity caused by the three-side-view under stressful condition such as video-delayed condition. The difficulty of the spatial recognition caused the declination of robot drivability and inclination of incongruousness in given view. The three-side-view presentation method would be able to support relative location/posture recognition, but the complexity of three-side-view could cause difficulty of spatial recognition and robot control.

CONCLUSION

In this research, the three-side-view presentation method was proposed. The three-side-view can present relative location/posture precisely.

The effect of the three-side-view was evaluated. As the results of the experiment, the three-side-view presentation did not affect for operation time under a teleoperation task with delayed video presentation. For accurate pointing task, the three-side-view presentation improved the accuracy of the final posture of surgical instruments. As sensory impression of a surgeon, the three-side-view would be a

little helpful but a little complex in spatial recognition. The three-side-view presentation was effective for accurate pointing task.

The complexity of the spatial recognition could cause difficulty of robot control. For effective support of spatial recognition in telesurgery, the evaluations of other presentation methods are required. In future research, effective presentation methods and video switching strategies in optimum timing should be studied for supporting spatial recognition of a teleoperating surgeon under video-delayed environment.

REFERENCES

1. Hori, K., Oyama, H., Ozaki, Y., Tsuda, T., Suenaga, T., Kuroda, T., Suga, M., Komori, M., Oshiro, O., Minato, K., Chihara, K., and Takahashi, T., Surgical cockpit system and effectiveness of its immersive environment. *Comput. Assist. Radiol. Surg.* 1160, 2001.
2. http://www.ai3.net/
3. Nagasawa, S., *Analysis of Cyclic Paired Comparison AHP with Logarithmic Linear Model.* Annual Conference of the Operations Research Society of Japan 1994 Autumn, pp. 34–35, 1994 (in Japanese).

Computer Methods and Programs in Biomedicine (2005) 80, 216–224

ELSEVIER

Computer Methods and Programs in Biomedicine

www.intl.elsevierhealth.com/journals/cmpb

Interaction model between elastic objects for haptic feedback considering collisions of soft tissue

Yoshihiro Kuroda[a,*], Megumi Nakao[b], Tomohiro Kuroda[c], Hiroshi Oyama[d], Masaru Komori[e]

[a] *Graduate School of Medicine, Kyoto University, Yoshida-Konoe-cho, Sakyo, Kyoto 606-8501, Japan*
[b] *Graduate School of Information Science, Nara Institute of Science and Technology, Takayama 8916-5, Ikoma, Nara 630-0192, Japan*
[c] *Department of Medical Informatics, Kyoto University Hospital, 54 Kawahara-cho, Shogoin, Sakyo, Kyoto 606-8507, Japan*
[d] *Graduate School of Medicine, The University of Tokyo, 7-3-1, Hongou, Bunkyo, Tokyo 113-8655, Japan*
[e] *Computational Biomedicine, Shiga University of Medical Science, Tsukiwa-cho, Seta, Otsu, Siga 520-2192, Japan*

Received 10 February 2004; received in revised form 12 July 2005; accepted 8 September 2005

KEYWORDS
Virtual reality;
Medical simulation;
Haptic display;
Elastic body;
Interaction

Summary The simulation of organ–organ interaction is indispensable for practical and advanced medical VR simulator such as open surgery and indirect palpation. This paper describes a method to represent real-time interaction between elastic objects for accurate force feedback in medical VR simulation. The proposed model defines boundary deformation of colliding elements based on temporary surface forces calculated by temporary deformation. The model produces accurate deformation and force feedback considering collisions of objects as well as prevents unrealistic overlap of objects. A prototype simulator of rectal palpation is constructed on general desktop PC with a haptic device, PHANToM. The system allows users to feel different stiffness of a rear elastic object located behind another elastic object. The results of experiments confirmed the method expresses organ–organ interaction in real-time and produces realistic and perceivable force feedback.

1. Introduction

Virtual reality (VR) technologies enable physicians to interact with flexibly customized simulated environments based on visual, auditory and haptic feedback without potentially harmful contact with real patients. For this reason, VR-based simulation has

* Corresponding author at: Department of Medical Informatics, Kyoto University Hospital, 54 Kawahara-cho, Shogoin, Sakyo, Kyoto 606-8507, Japan. Tel.: +81 75 751 3165; fax: +81 75 751 3077.
E-mail address: ykuroda@kuhp.kyoto-u.ac.jp (Y. Kuroda).

0169-2607/$ – see front matter © 2005 Elsevier Ireland Ltd. All rights reserved.
doi:10.1016/j.cmpb.2005.09.001

attracted considerable attention as a key technology for the advancement of medical treatments and improvement of quality of human life. In the field of medicine, VR simulators are applied for uses such as education, therapy and rehabilitation, procedural training, surgical planning, rehearsal, and interoperative support [1,2]. Though many simulators have been developed, and a few even commercialized [3–6], most have dealt with single organ objects without handling collisions between multiple organ objects [4–9]. This makes them unsuitable for VR simulation of the human body, a system with many organs which often collide. Haptic feedback is especially important in delicate surgical pressures requiring fine sensations, especially when slightly excessive pressure can injure a patient. Haptic sensation is also significant in palpation: as the physician examines the characteristics of an organ beneath the body surface with the tips of his or her fingers, collisions of the soft tissues are inevitable. This paper proposes a model of interaction between soft tissues, in order to provide a virtual environment simulating haptic feedback from the collisions of soft tissues.

Palpation and surgery simulations require the use of physics-based deformable models to accurately calculate the deformation and force caused by physical action on soft tissue. This adds considerably to the challenge of simulation, however, as physics-based deformation models generally require more computations than the geometry-based deformation models used in computer graphics. A comprehensive simulation of multiple characteristics of soft tissue all at once is tremendously difficult. Elasticity, a property related to force and displacement, is one of the most important characteristics of soft tissue. Accordingly, this paper treats soft tissues as elastic objects and seeks to model the interactions between them. The interaction model presented here must perform three important functions.

1. To allow interactive manipulation in real-time.
2. To take into account the physical properties of colliding objects.
3. To produce an adequate visual reality.

Interactive manipulation, an operation performed in both palpation and surgery, requires real-time computation of soft tissue deformation and reaction forces. When a soft elastic object and a hard object collide, the former deforms more, as shown in Fig. 1. In addition, the reaction forces during the collision depend on the extent of the deformations in the collision area. Thus, the interaction model must represent the deformation on the basis of the physical properties of both elastic objects. Visual reality is one of the most important functions for effective simulation. Excessive invasion of colliding objects must be avoided.

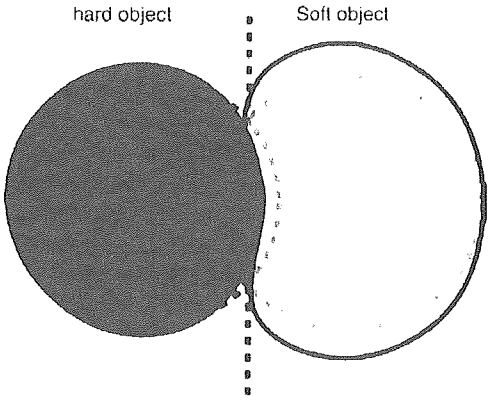

Fig. 1 Deformation caused by collision of elastic objects with different stiffnesses. The soft object deforms more than the hard object.

In this paper, we propose an interaction model between elastic objects that performs the above functions. After describing the proposed model, we evaluate its performance and validity by applying it to the development of a rectal palpation simulator.

2. Background

The simulation of physical phenomena has been a key technology to enhance visual and haptic reality in medical simulations. Studies in biomechanics and computer graphics in the field have devoted particularly close attention to soft tissue modelling [10–13]. Many kinds of physics-based deformable models have been proposed for deformation and force feedback [13–19]. One such model, the mass-spring model, represents an object as points of mass joined by springs [15,16]. Though effectively applied for a variety of uses, the model does not perform adequately when simulations require accurate calculation of deformation and reaction force [7]. The mass-spring model also requires fine-tuning of physical parameters to represent certain physical characteristic, and improper parameter values lead to system instability. The boundary element model (BEM) and long element model (LEM) have also been proposed for deformation and force feedback. Though both are capable of fast computation [12,17,18], they have limitations in surgical and palpation simulations. An organ with internal lesions possesses several distinct physical properties, yet BEM assumes that an organ is homoge-

neous. Organs also tend to be complex in shape, yet LEM is poor at representing anything but simple shapes. A fourth alternative, the finite element (FE) model, has been regarded as the most accurate model for many years, but it is also the most computationally expensive [19]. Thankfully, recent progress of computers and computational methods has improved the outlook. With innovations such as condensation and Hirota's method [19,20], computation and simulation with haptic interaction can now be performed in real-time by the FE method.

Thousands of studies in mechanical engineering and VR have focused on the interaction between elastic objects. None, however, have been able to theoretically solve the contact problem. While the Hertz theory [21] is sometimes applied to the contact problem for convenience, it cannot be applied for arbitrary shapes. In VR simulation, several methods for describing collision responses have been proposed for the modelling of interactions between elastic objects [22,23]. Sibille et al. solve the contact problem by projecting colliding nodes to a plane which passes the barycenter of the colliding nodes and is oriented perpendicularly to the average normal vector of the colliding nodes (see Fig. 2) [22]. Though effective in curtailing the invasion of colliding objects, this method models deformation and haptic force based on geometrical information rather than information on the actual physical properties of the objects. Joukhadar et al. apply forces proportional to the invading volume of colliding objects onto the surfaces of the objects [23]. Their method fails to consider the physical properties of the volume, however, and it does not permit real-time computation of the invading volume (as they describe in their paper). Overall, the existing methods do not seem to provide adequate solutions for the above functions.

None of the rectal palpation simulators so far developed [24,25] have attempted to simulate the deformation and interaction between the rectum and prostate. This functional limitation compromises the flexibility of the simulation conditions and obfuscates the visual and haptic realities.

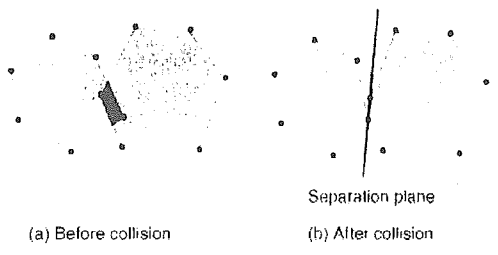

Fig. 2 Geometrical interaction model by Sibille et al.

3. Design considerations

There are two ways to represent multiple organs: with a single elastic object representing multiple organs or with multiple elastic objects representing multiple organs.

Several simulators [26,27] use the former method, treating multiple organs as a single elastic object. Methods which rely on the filling of finite elements into gaps between elastic objects are unsuitable in situations where contact regions often change. When the contact regions of organs are changed, the topology of each object changes and the global stiffness matrix needs to be reassembled. It also becomes necessary to re-compute the pre-processing stage, including the inversion of the global stiffness matrix [20]. This presents a significant problem, as the re-computation is generally slower than the haptic refresh rate (about 300 Hz) [2]. As an added problem, limitations in storage volumes would make it extremely difficult to pre-compute and store all of the possible models. Given the representation capabilities and resources of today's computers, we conclude that multiple organs must be modelled as multiple independent objects.

4. Computational methods

4.1. Interaction model between elastic objects

Our interaction model between elastic objects focuses on physics-based force feedback taking into account the physical properties of colliding objects. We define "interaction" as the process which determines the deformation in the collision area based on the physical properties of the colliding objects. Though the extent of deformation by collisions is theoretically unsolved, as mentioned earlier, it presumably depends on the physical properties of the colliding objects. Thus, the deformation is determined based on surface forces temporarily calculated by specifying temporary displacements, where surface forces are derived from physical properties and can be calculated rapidly by the finite element method using Hirota's model [20]. Collisions are detected by testing whether a node has moved into the internal side of the surface of another object.

The illustration in Fig. 3 outlines the proposed model. The actual displacements of the colliding elements of object A, B are calculated as $|\vec{b}| : |\vec{a}|$. The displacements are thus given to the elements

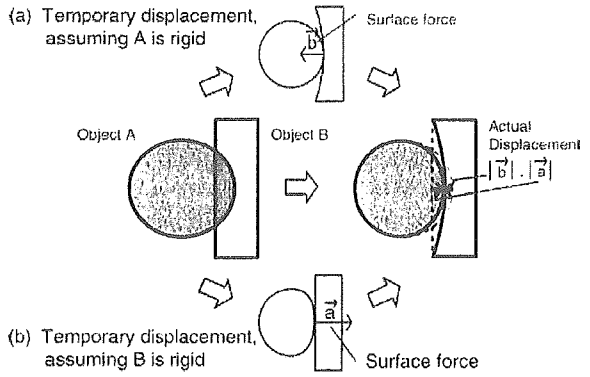

Fig. 3 Interaction model between elastic objects. Object A is regarded as a rigid body and surface force $\vec{b}$ is calculated on object B (see (a)). Object B is regarded as a rigid body and surface force $\vec{a}$ is calculated on object A as well (see (b)). The actual displacements of the colliding elements of object A, B are calculated as $|\vec{b}| : |\vec{a}|$ and given to the elements and transferred.

and the elements are transferred, as the surface forces indicate the degree of resistance to invasion of the colliding objects.

4.2. Calculation of interaction

The calculation of interaction consists of the following procedures:

1. Detection of colliding elements.
2. Calculation of temporary displacements.
3. Temporary deformation.
4. Calculation of temporary surface forces.
5. Calculation of actual displacements.

The temporary deformation and the temporary surface forces are based on the finite element method, a method which produces accurate deformation and reaction forces. The simulation in this study represents soft tissue as tetrahedral meshes. The detection of the colliding elements depends on the collision detection algorithm. The calculation of interaction depends on external methods, as shown in Fig. 4.

The steps in each procedure are outlined below.

- Detection of colliding elements.
  Collisions are checked by testing whether a node has moved inside a polygon of another object. If collisions are detected on both sides of the objects, the following procedures are carried out.
- Calculation of temporary displacements.
  If a collision between a node 'X' of object A and a polygon 'S' of object B is detected, the polygon S is displaced perpendicularly, as shown in Fig. 5.

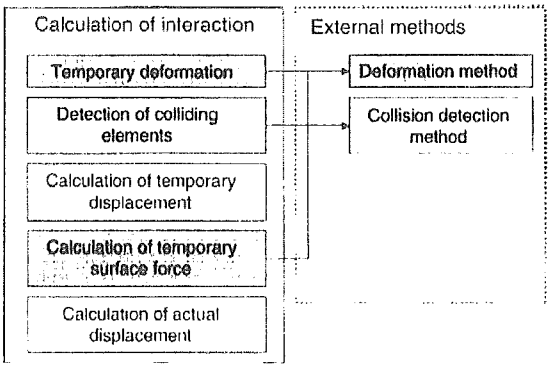

Fig. 4 The components of the interaction method and their dependence on the deformation and collision detection methods.

The vector of temporary displacement $\overrightarrow{u_{temp\_B}}$ is:

$$\overrightarrow{u_{temp\_B}} = \overrightarrow{FX} \tag{1}$$

where F is the perpendicular foot of nodes X to S.

Temporary displacements of nodes P, Q, and R are $\overrightarrow{u_{temp\_B}}$. The new positions, P′, Q′, and R′ are as follows.

$$\begin{aligned} \overrightarrow{P'} &= \overrightarrow{P} + \overrightarrow{u_{temp\_B}} \\ \overrightarrow{Q'} &= \overrightarrow{Q} + \overrightarrow{u_{temp\_B}} \\ \overrightarrow{R'} &= \overrightarrow{R} + \overrightarrow{u_{temp\_B}} \end{aligned} \tag{2}$$

In the same way, a temporary displacement $\overrightarrow{u_{temp\_A}}$ is calculated and given to the polygon of object A.

- Temporary deformation.
  The temporary deformation is calculated based on the finite element method using Hirota's model [20] with temporary displacements.
- Calculation of temporary surface forces.

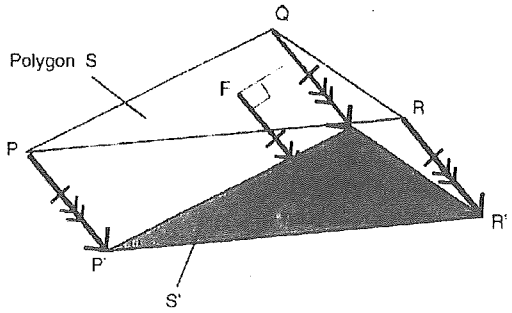

Fig. 5 Temporary displacement of the polygon. The polygon S is transferred perpendicularly with distance between the points F and X.

A temporary surface force $\vec{f}$ of polygon S is defined as an average vector of nodal forces on P′, Q′, R′:

$$\vec{f} = \frac{\vec{f_P} + \vec{f_Q} + \vec{f_R}}{3} \quad (3)$$

where $\vec{f_P}, \vec{f_Q}, \vec{f_R}$ are the nodal forces on P′, Q′, R′. This calculation gives the temporary surface forces based on the stiffnesses.

- Calculation of actual displacements.

  Actual displacements of colliding elements of the object A, B are calculated as $|\vec{f_B}| : |\vec{f_A}|$ and given to the elements, as surface forces indicate the degree of resistance to invasion of colliding objects.

To visualize the contact boundary of the colliding area realistically, the simulation displaces the polygon of only one object and the node of another object, instead of displacing the polygons of both objects. The sum of the displacements of the polygon and the node are $\overrightarrow{u_{temp\_B}}$. The node is positioned on the polygon. Accordingly, this method avoids invasion and separation between the polygon and node. It also reduces the computation of the finite element method, as the displacement of only one polygon instead of two results in the displacement of fewer nodes (three nodes are displaced for each polygon). Displacements $\vec{u_A}$ and $\vec{u_B}$ of colliding elements of object A, B are as follows:

$$\vec{u_A} = -\frac{|\vec{f_B}|}{|\vec{f_A}| + |\vec{f_B}|}\overrightarrow{u_{temp\_B}} \quad (4)$$

$$\vec{u_B} = \frac{|\vec{f_A}|}{|\vec{f_A}| + |\vec{f_B}|}\overrightarrow{u_{temp\_B}} \quad (5)$$

where $\overrightarrow{u_{temp\_B}}$ is a vector of temporary displacements, $\vec{f_A}$ and $\vec{f_B}$ are surface forces on the colliding polygons of object A, B, respectively, $\vec{u_A}$ is given to the node of object A, and $\vec{u_B}$ is given to the component nodes of the polygon of object B.

This method enables us to determine the deformations in the collision area with due consideration of the physical properties of the colliding objects.

5. System description

5.1. Structure of the system

As previously mentioned, collisions between multiple organs are especially important to consider in the haptic displays of palpation simulations. Our group addresses this challenge by developing a rectal palpation simulator and using it to evaluate the proposed model. Rectal palpation is a very common and important manipulation in urology. A physician inserts his or her index finger through the anus of the patient and palpates the prostate gland indirectly through the rectal wall to assess the condition of the gland.

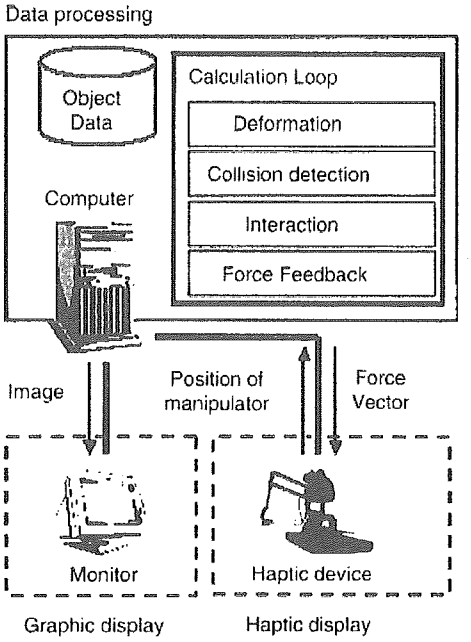

Fig. 6 Structure of the rectal palpation simulator. The figure shows the three system components used to simulate organ–organ interaction with a haptic display: a data processing unit, graphic display unit, and haptic display unit. The data processing unit interacts with the other units.

Fig. 6 illustrates the structure of our rectal simulator system. The system consists of a graphic part, a haptic part, and a data processing part. The data processing program is coded in Visual C++ and run on a general computer with dual Pentium III 933 MHz CPUs and 1 GB of main memory. The system is equipped with a PHANToM Premium 1.0A haptic device (SensAble Inc., Woburn, MA).

Organ object data are generally obtained from medical imaging modalities such as CT, MRI, and cross-sectional images. *Amira*™ (Mercury Computer Systems Inc. [28]) semi-automatically segments the data and divides them into tetrahedral elements for finite element computations, and stores geometry data such as vertices (nodes), tetrahedrons, and surface triangles (polygons). Real-time simulation with haptic display is achieved by applying a static and linear model and fast computation techniques such as condensation [19] and Hirota's method [20].

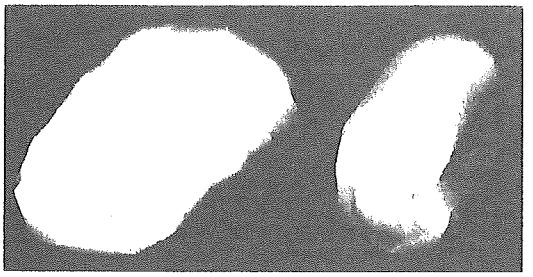

Fig. 7 Rectal object (left) and prostate object (right) used for the rectal palpation simulation.

Table 1 Finite element representation of objects

Model	Total nodes (free surface nodes)	Tetrahedron
Rectum	282 (207)	889
Prostate	360 (110)	1312

Inverse stiffness matrices representing the stiffness of objects are pre-computed and stored for the physics simulation. The manipulator position is updated from a haptic device. The reaction force, a parameter calculated in the physics simulation, is conveyed to the user kinaesthetically via the haptic device.

5.2. Modelling of objects

Fig. 7 shows the rectal and prostate objects, the principal objects in the simulation of rectal palpation. The rectal object is re-constructed from RGB data from the Visible Human Dataset [29]. The prostate object is generated by piling up cross-sectional images of the prostate. Table 1 shows the number of nodes in the finite element representation of the objects. The "free surface nodes" are non-fixed nodes located on the surface.

A Poisson ratio of 0.40 is given to both objects in view of the high water content and low compressive features of human organs [30]. A Young modulus of 1.0 MPa is given to the rectal object and 1.0 and 5.0 MPa are given to two types of prostate objects, respectively, one representing a normal prostate and the other representing a hardened gland.

6. Status report

6.1. Calculation time

We examined the calculation time when a sphere-shaped object A and cubic object B collide. Both objects are in contact and a moving point pushes a point of object A from the opposite side of the contact region. The calculation times for deformation, interaction, and total computation of one cycle are shown in Fig. 8.

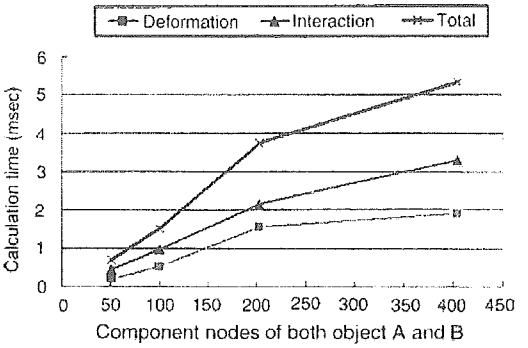

Fig. 8 Calculation times for deformation, interaction, and total computation. The total calculation time for the two 200-noded objects, less than 4 ms, indicates that the method is applicable to objects up to this scale and level of complexity.

The horizontal axis indicates the number of component nodes of both objects A and B. The vertical axis indicates the calculation time (ms). Only about 10% of the nodes of both objects are fixed, hence 90% of the total are free nodes on the surface.

As the graph shows, the time duration of the deformation and interaction increases linearly with the number of nodes. The time required for total computation reaches 4 ms, the limit for stable haptic feedback with this stiffness, when the object has approximately 200 component nodes.

By omitting calculation for regions where the deformation effects are trivial, however, it becomes possible to simulate collisions between two objects with more than 200 nodes within the 4 ms limit. The calculation times for deformation, interaction, and total computation in the rectal palpation simulator without this omission are 1.17, 1.62, and 2.88 ms, respectively.

6.2. Experiments based on simulation

The experiment verifies that the stiffness of a neighbouring object which cannot be touched directly (in this case prostate object) affects the value of the reaction force. Fig. 9 shows a view of the simulation.

In this experiment, the simulator moves the point of manipulation from the initial position towards the prostate object to a depth of 0.5 cm and then calculates the reaction force imposed on the point. The simulation is carried out under three simulated prostate conditions.

Condition 1: No prostate object is set.

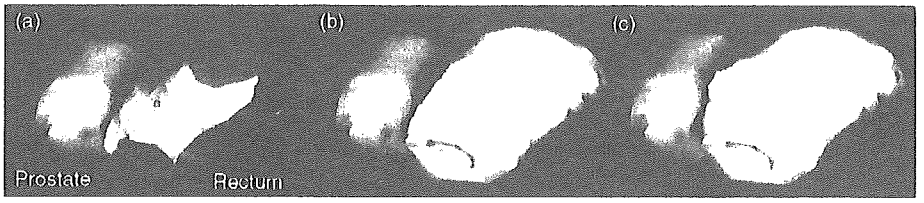

Fig. 9 Simulation view of the rectal palpation simulator. (a) The rectal object is displayed transparently. The sphere in the center of the image is a point of manipulation located in the initial position. (b) The two objects are located in the initial position. (c) The point of manipulation pushes the inner wall of the rectal object towards the neighbouring prostate object, resulting in the deformation of both objects.

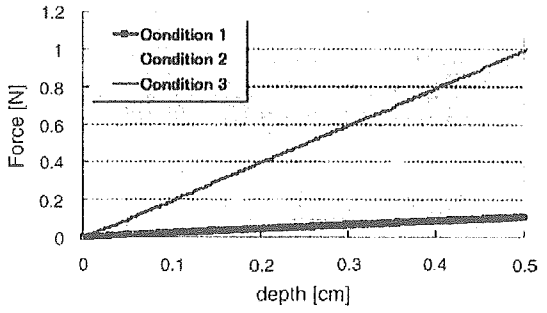

Fig. 10 Reaction forces produced by the proposed model. The forces produced under condition 2 (the softer prostate object) and condition 3 (the harder prostate object) differ in the virtual environment.

Condition 2: Soft prostate object (1.0 MPa Young modulus) is set.
Condition 3: Hard prostate object (5.0 MPa Young modulus) is set.

Soft and hard prostate objects represent a regular prostate gland and a hardened prostate gland due to cancer, respectively.

Fig. 10 shows the values of the haptic forces in each case when applying the proposed model. Fig. 11 shows the values in the model proposed by Sibille et al. [22] (mentioned in Section 2).

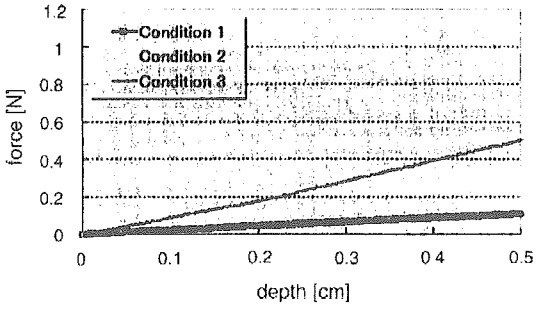

Fig. 11 Reaction force produced by Sibille's model. The forces produced under conditions 2 and 3 are almost identical.

The horizontal axis represents the depth (cm) of pushing of the rectal object and the vertical axis represents the haptic force (N), a parameter which takes a positive value when the force opposes the direction of the pushing. The thick black, white, and grey lines indicate the forces produced under conditions 1, 2, and 3, respectively. In the case of Sibille's model [22], the forces produced under conditions 2 and 3 are almost the same. As a consequence, the plotted lines for conditions 2 and 3 overlap in Fig. 11.

As seen in Fig. 10, the forces produced under conditions 2 and 3 differ when applying our newly proposed model. Simply put, the hard prostrate object produces a stronger force than the soft one. On the other hand, the Fig. 11 shows that with the Sibille's model the forces of both cases do not differ. The greater hepatic force produced by this model under condition 3 can be attributed to the consideration of the stiffness of the neighbouring object within this model.

6.3. Subjective experiments

Our subjective experiments confirmed that human examiners can perceive a difference in force based on consideration of the stiffness of a neighbouring object.

The examinations were performed by 15 medical students with no experience in using haptic devices. The examiners were asked to distinguish the stiffness of prostate objects through haptic sensation with their dominant hands. Each examiner touched the prostate object indirectly under conditions 2 and 3 (simulated by the system in random order), then indicated which felt harder. An indication that the hard prostate model (condition 3) felt harder was considered the correct answer. Each examiner performed four tests in each interaction model; the proposed model and the existing model by Sibille et al. [22].

To prevent the movement and position of the hand from influencing the result, the bottom of the

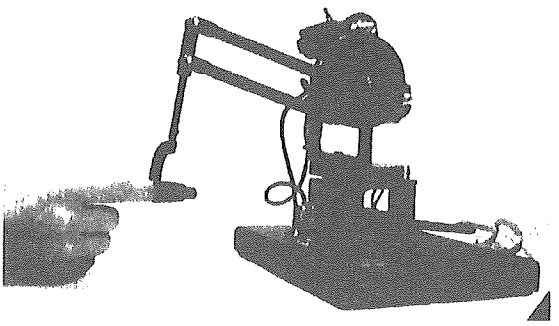

Fig. 12 Hand position and manipulation protocol during the experiments.

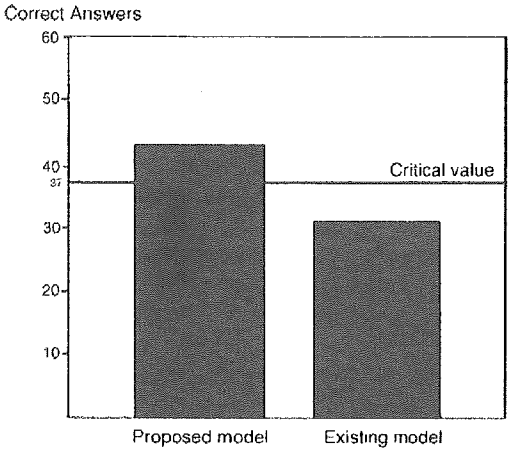

Fig. 13 Results of experiments.

dominant hand was fixed on the desk in a position that enabled leftward and rightward movement of the forefinger, as shown in Fig. 12.

The recorded differences in hand sensations between the hard and soft prostate conditions were tested for each model by a pair test at $p < 0.05$. Fig. 13 shows the experimental results. The critical value, defined as the value that a test statistic must exceed to reject the null hypothesis, was 37 out of 60 samples. In the tests using the proposed model, 43 out of 60 answers were correct (exceeding the critical value). In the tests using Sibille's model, only 31 out of 60 answers were correct (falling below the critical value). We thus confirmed that the proposed model can represent the forces on the basis of the stiffness of a neighbouring object in a manner that people can perceive.

7. Lessons learned and future plans

Nakao et al. [31] have reported that skilled cardiovascular surgeons can accurately recall and identify the relative levels of stiffness of a normal aorta and hardened aorta through the sense of touch. In the present experiments using a simulator of rectal palpation, we had the tests performed by skilled urologists on the assumption that they could accurately recall the tactile sensations of the fingertip when pushing the prostate through the rectal wall. Their answers indicated that the sensation of pushing the simulated prostate object was similar to the real sensation. One examiner commented, however, that the sensation of the simulated prostate examination was more realistic when the rectal object could be smoothly stroked. This seemed to be due to the low resolution of the rectal model, a limitation which resulted in large changes in the direction of the force vector. In the future it will be desirable to develop an efficient algorithm of the proposed model and apply a multiresolution method to reduce computations. In any case, the results of our evaluation suggest that the proposed model produces realistic haptic force when the examiner pushes organs. Needless to say, however, further improvement of the system is desirable.

Physicians have also suggested that the palpation simulator would be useful to discuss with many physicians, now that recent trends to promote patient rights have reduced the opportunities for more than three physicians to palpate the same patients. Moreover, the detection of internal lesions of the prostate facilitates advanced diagnosis. The proposed system also allows the setting of different physical parameters inside organs. Thus, a future focus of study will be the application of this palpation system with an internal lesion model.

This paper proposed an interaction model for colliding elastic objects designed to produce haptic feedback in consideration of the physical properties of the colliding objects. The interaction model determines boundary deformations by calculating temporary displacements and enables the calculation of the reaction force on the basis of the physical properties of the colliding organ objects. The simulation results confirmed that the proposed method could simulate collisions of two 200-noded FEM objects in real-time. Subjective evaluation using a rectal palpation simulator implementing the proposed method confirmed that the proposed method could express the difference of stiffness of a rear object hidden behind another elastic object in a manner perceivable to a human being. The method will be useful for advanced simulators requiring accurate visual and haptic feedback.